Magnetoelastic coupling forbidden by time-reversal symmetry: Spin-direction-dependent magnetoelastic coupling on MnO, CoO, and NiO

Sanghyun Lee,[1,*] Yoshihisa Ishikawa,[1] Ping Miao,[1,2] Shuki Torii,[1,3] Toru Ishigaki,[4] and Takashi Kamiyama[1,2,3,†]

[1]*Institute of Materials Structure Science, KEK, Tokai 319-1106, Japan*

[2]*Sokendai (The Graduate University for Advanced Studies), Tokai 319-1106, Japan*

[3]*J-PARC Center, KEK, Tokai 319-1106, Japan*

[4]*Frontier Research Center for Applied Atomic Science, Ibaraki University, Tokai 319-1106, Japan*

(Received 4 November 2015; revised manuscript received 1 February 2016; published 24 February 2016)

In the Landau free energy, which is a powerful tool for describing the physical properties and phase transitions in condensed-matter physics, it has been generally believed that time-reversal symmetry allows only even-power polynomials in the magnetic moment when magnetic transition happens. Although no experimental evidence supports it, this symmetry constraint is very strict in theory. On the other hand, MnO, CoO, and NiO have been extensively studied for several decades since these materials are used to test advance experimental and theoretical methods. However, their precise spin directions and phase-transition mechanism have remained as a long-standing problem until now. To resolve these issues, we used the cutting-edge time-of-flight neutron powder diffractometer (SuperHRPD) at the Japan Proton Accelerator Research Complex (J-PARC) to study the spin-direction-dependent magnetoelastic coupling in MnO, CoO, and NiO. We also constructed a group-subgroup structure relation from Fm-3m to $C2/m$ with exchange striction and a type of magnetostriction (dipolar and roto magnetostriction). These unified viewpoints and the high-resolution neutron powder diffractometer enable us to construct an order-parameter vector diagram. The order-parameter vector diagram reveals distinguished order-parameter coupling and phase-transition characters by different $\Gamma_1^+(A_g)$ and $\Gamma_2^+(B_g)$ spin direction. Moreover, the experiment results show clearly that the CoO_6 octahedral distortion and the Co magnetic moment couple through a magnetoelastic coupling $\epsilon_{\rm oct} \sim M^3$, which is forbidden by time-reversal symmetry but allowed by the more general magnetic symmetry—the so-called rotation-time-reversal symmetry in the double antisymmetry space group. Rotation-time-reversal symmetry allows the coupling of odd-power polynomials in the spin vector and odd-power ones in the roto vector when both spin- and roto-axial vectors belong to the same irreducible representation in Landau free energy. Here, we show experimental evidence that the magnetic order parameter and static structural order parameter belong to the same irreducible representation in the materials. Experimental discovery of general magnetic symmetry opens a way to find the physics forbidden by time-reversal symmetry in condensed matter physics.

DOI: 10.1103/PhysRevB.93.064429

I. INTRODUCTION

Symmetry is a key concept for understanding the physical properties, interactions, and phase transitions in condensed-matter physics. To apply this concept to phase transitions, the Landau free energy is Taylor expanded in the order parameter near the phase-transition point and the free-energy term is required to be invariant under symmetry operations of the high-symmetry parent group. This Landau free energy is extremely useful and flexible for investigating the phase transition and physical properties in various systems. For example, it has been generally believed that time-reversal symmetry allows only even-power polynomials in the magnetic moment in the Landau free energy when magnetic phase transition occurs [1,2]. To date, discussions of magnetism in condensed-matter physics have been guided by this strong theoretical symmetry constraint despite a lack of experimental evidence to justify it. However, if instead of time-reversal symmetry a new symmetry operation is shown experimentally to reverse the magnetic moment, then this issue must be revisited.

Gopalan and Litvin introduced rotation-reversal symmetry 1*, which reverses the time-independent axial vector (the so-called roto vector R) [3]. It differs from the well-known time-reversal symmetry 1′, which reverses the time-dependent axial vector (the so-called spin vector S). In addition, the direct product between rotation-reversal symmetry 1* and time-reversal symmetry 1′ gives rotation-time-reversal symmetry 1′*, which reverses both roto vector R and spin vector S: $1^*R = -R$, $1^*S = S$; $1'R = R$, $1'S = -S$; $1'^*R = -R$, $1'^*S = -S$ as shown in Fig. 1. These symmetries give rise to 17 803 double antisymmetry space groups (DASGs) that are derived from 230 conventional space groups [4,5]. Theoretically, magnetic moment can be reversed by not only time-reversal symmetry 1′ but also rotation-time-reversal symmetry 1′*. Thus, it is necessary to discuss possible polynomials in magnetic moment in Landau free energy by rotation-time-reversal symmetry. And then, it is important to prove experimentally which one is general magnetic symmetry between time-reversal symmetry 1′ and rotation-time-reversal symmetry 1′* since change in magnetic symmetry will give different symmetrical constraints in condensed matter physics.

On the other hand, transition-metal monoxides (TMOs), such as MnO, CoO, and NiO, have long-standing problems such as precise spin direction [6–26], a discontinuous or continuous phase-transition problem [27–42], and a

*lee@post.j-parc.jp

†takashi.kamiyama@kek.jp

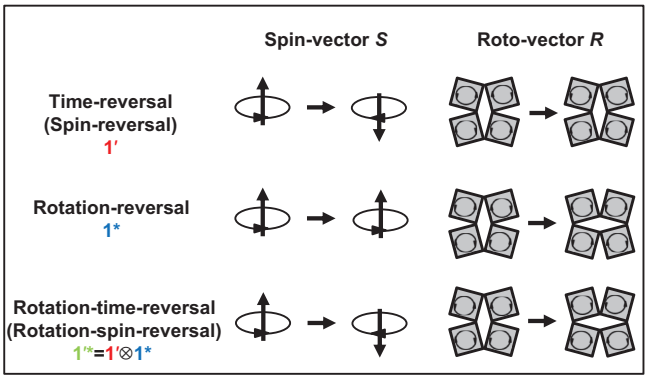

FIG. 1. In the double antisymmetry space group, $1'$ time-reversal, 1^* rotation-reversal, and $1'^*$ rotation-time-reversal symmetry operation on the time-dependent axial vector (spin vector S) and time-independent axial vector (roto vector R), respectively: $1'S = -S$, $1'R = R$, $1^*S = S$, $1^*R = -R$, $1'^*S = -S$, $1'^*R = -R$.

phase-transition mechanism [9,11,16,20,27,42–47]. TMOs have simple rocksalt structure Fm-3m in the paramagnetic state. Antiferromagnetic ordering causes stress, which induces structural distortion at the same temperature. Since antiferromagnetic ordering induces the simultaneous formation of ferroelastic twin domains, single-crystal neutron diffraction has difficulty determining the precise spin direction without detailed knowledge of the domain population [12,19]. Meanwhile, phase-transition theory expected discontinuous phase transition on MnO, CoO, and NiO [16,27–30]. MnO discontinuous phase transition is consistent with theoretical expectation [31–33,35,36,42]. However, at least, NiO indicates continuous phase transition within experimental resolution [34,36,37,39,41]. CoO phase transition is unclear and depends on sample preparation from different research groups [16,36,38–40]. Because of the theoretical background, it has been believed that CoO phase transition is very weak discontinuous phase transition, smaller than experimental resolution [16]. In addition, classical magnetostriction [16,44] and spin-driven Jahn-Teller distortion [9,11,42,47] are proposed theoretically for the CoO phase-transition mechanism. But, it is lacking experimental support at present, whereas in MnO and NiO phase-transition mechanisms it is generally accepted that exchange striction induces R-3m crystal structure [45,46]. However, exchange striction is insufficient to explain why MnO and NiO phase transitions are different within experimental resolution [6].

In this study, we resolve the issue of general magnetic symmetry and the long-standing problem of TMOs. In Sec. II, the theoretical and experimental methods are given. In Sec. III, we discuss possible polynomials of magnetic moment in Landau free energy with time-reversal symmetry and rotation-time-reversal symmetry. We also construct the TMOs group-subgroup structural relation with exchange striction and magnetostriction. This approach gives common crystal structure $C2/m$ with magnetic propagation vector k_m=(0 1 0.5). In Sec. IV, we demonstrate very-high-resolution time-of-flight neutron powder-diffraction results and discuss spin-direction-dependent magnetoelastic coupling. In Sec. V, we summarize the physical meaning of experimental results and the importance of general magnetic symmetry.

II. METHOD

To avoid the twin-domain problem, we use time-of-flight neutron powder-diffraction measurements performed at the cutting-edge super-high-resolution powder diffractometer (SuperHRPD) [48,49] of the Japan Proton Accelerator Research Complex (J-PARC) to measure the crystal- and magnetic-order parameters simultaneously. In principle, when monoclinic distortion exceeds the diffractometer resolution, high-resolution powder neutron diffraction makes it possible to not only obtain clear crystal and magnetic structures but also easily measure order-parameter coupling. We used commercial powder samples MnO 99%, CoO 99.99%, and NiO 99.999% from Sigma Aldrich. We employ a cryostat to maintain MnO and CoO at low temperature and a furnace to maintain NiO at high temperature. After obtaining the instrument parameter by Z-Rietveld software [50,51], we used the Fullprof software [52] to perform Rietveld analysis on a high-resolution backscattering bank. We also used BasIreps [52], SARAh [53], Bilbaocrystallographic server [54], and the International table of crystallography Vol. A1 [55] to apply the group representation theory, analyze the magnetic symmetry, and construct the group-subgroup family trees. Measurements of CoO show that the Néel temperature is 10 K

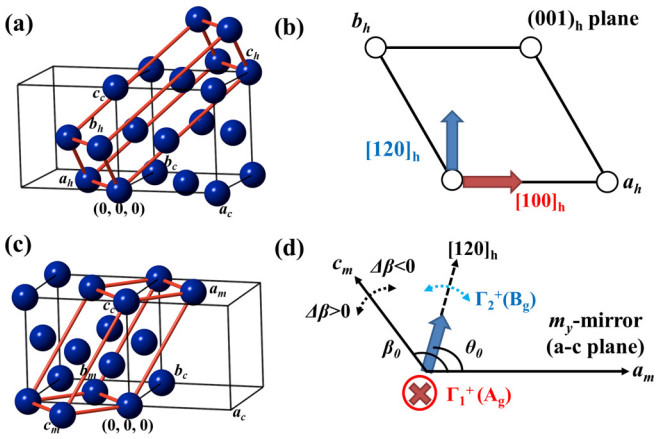

FIG. 2. TMO spin direction in R-3m and $C2/m$. (a) R-3m hexagonal lattice transformation $(a_h,b_h,c_h) = (-a_c/2 + b_c/2, -b_c/2 + c_c/2, a_c + b_c + c_c)$ from Fm-3m cubic lattice with a_c, b_c, and c_c. For clarity, only transition metals are shown, whereas oxygen is omitted. (b) Two spin-basis vectors: the $[100]_h$ and $[120]_h$ spin directions (red and blue arrows, respectively) compose the easy-plane spin direction inside the R-3m $(001)_h$ hexagonal plane. These spin directions break the threefold crystal symmetry and induce the maximal subgroup $C2/m$. (c) $C2/m$ monoclinic lattice transformation $(a_m,b_m,c_m) = (a_c/2 + b_c/2 + c_c, -a_c/2 + b_c/2, -a_c/2 - b_c/2)$ from Fm-3m cubic lattice with a_c, b_c, and c_c. (d) Two spin directions $\Gamma_1^+(A_g)$ and $\Gamma_2^+(B_g)$ (red and blue arrows, respectively) in $C2/m$. The R-3m $[100]_h$ spin direction transforms to the $\Gamma_1^+(A_g)$ spin direction, which is always fixed along the monoclinic b axis in $C2/m$. In contrast, the R-3m $[120]_h$ spin direction transforms to the $\Gamma_2^+(B_g)$ spin direction with the initial spin angle $\theta_0 = \cos^{-1}(1/3) \approx 70.5288^\circ$, which is rotated in the m_y mirror plane in $C2/m$. The initial monoclinic angle $\beta_0 = \cos^{-1}(-\frac{1}{\sqrt{3}}) \sim 125.2644^\circ$ is derived from paramagnetic cubic Fm-3m. The $\Gamma_2^+(B_g)$ spin direction and variation $\Delta\beta$ in the monoclinic angle are correlated.

higher than the reported transition temperature [42] because of the temperature gradient between the sample and the sensor position inside the cryostat when the sample is near room temperature. The observed higher Néel temperature does not affect the order-parameter coupling at a given temperature because temperature effects cancel out.

III. THEORY

A. Landau free energy

The DASG suggests that the spin vector S is reversed by applying either time-reversal symmetry $1'$ or rotation-time-reversal symmetry $1'^*$ [3–5]. Surprisingly, the new rotation-time-reversal symmetry $1'^*$ allows odd-power polynomials in the magnetic moment in the Landau free energy. Two possible theoretical cases exist wherein the S spin vector and R roto vector are ordered simultaneously. In the first case, S and R appear when $1'$ time-reversal symmetry and 1^* rotation-reversal symmetry are separately broken, i.e., $1'S = -S$, $1^*R = -R$. In this case, the Landau free-energy term must be invariant under $1'$ time-reversal symmetry and 1^* rotation-reversal symmetry operations individually. This is expressed by

$$F = F_0 + a_2S^2 + a_4S^4 + b_2R^2 + b_4R^4 + cS^2R^2 + \cdots . \quad (1)$$

S and R belong to different irreducible representations (irreps) and give the S^2R^2 coupling term. However, in the second case, both S spin vector and R roto vector appear together in breaking $1'^*$ rotation-time-reversal symmetry, i.e., $1'^*A = -A = (-S,-R)$ when S and R merge into a single irrep $A = (S,R)$. In this case, the Landau free-energy term must be invariant under the $1'^*$ rotation-time-reversal symmetry operation. This is given by

$$\begin{aligned} F &= F_0 + a_2A^2 + a_4A^4 + \cdots \\ &= F_0 + a_2S^2 + a_4S^4 + b_2R^2 + b_4R^4 \\ &\quad + c_1SR + c_2S^3R + c_3S^2R^2 + c_4SR^3 + \cdots . \end{aligned} \quad (2)$$

Additional terms that couple order parameters appear, such as SR, S^3R, and SR^3, which involve odd powers of the spin vector S and roto vector R which are forbidden by time-reversal symmetry $1'$ and rotation-reversal symmetry 1^* individually but are allowed here by rotation-time-reversal symmetry $1'^*$. In addition, rotation-time-reversal symmetry $1'^*$ reduces the number of condensed irreps in the phase transition.

The Landau free energy, including antiferrodistortive antiferromagnetic bilinear coupling, describes heat-capacity tails above T_N in multiferroic $BiFeO_3$ and $EuTiO_3$ [56]. When spin vector S and roto vector R change their signs simultaneously between sublattices, they argue that odd-odd power polynomials exist between spin vector and roto vector, while, here, rotation-time-reversal symmetry breaking gives a more strict constraint that both vectors must belong to the same irreducible representation. For instance, different spin direction causes distinguished roto-vector and spin-vector coupling in this study, but not in the approach taken in [56]. Octahedral rotations and antiferromagnetic order occur sequentially at different temperatures in the two perovskite materials, thus proving that order-parameter coupling is difficult to perform experimentally. Therefore, it is important to discern the type of order-parameter coupling in Eq. (1) or (2) and existence of spin-direction-dependent magnetoelastic coupling, where the spin vector S and roto vector R appear simultaneously at the same phase-transition temperature in suitable materials.

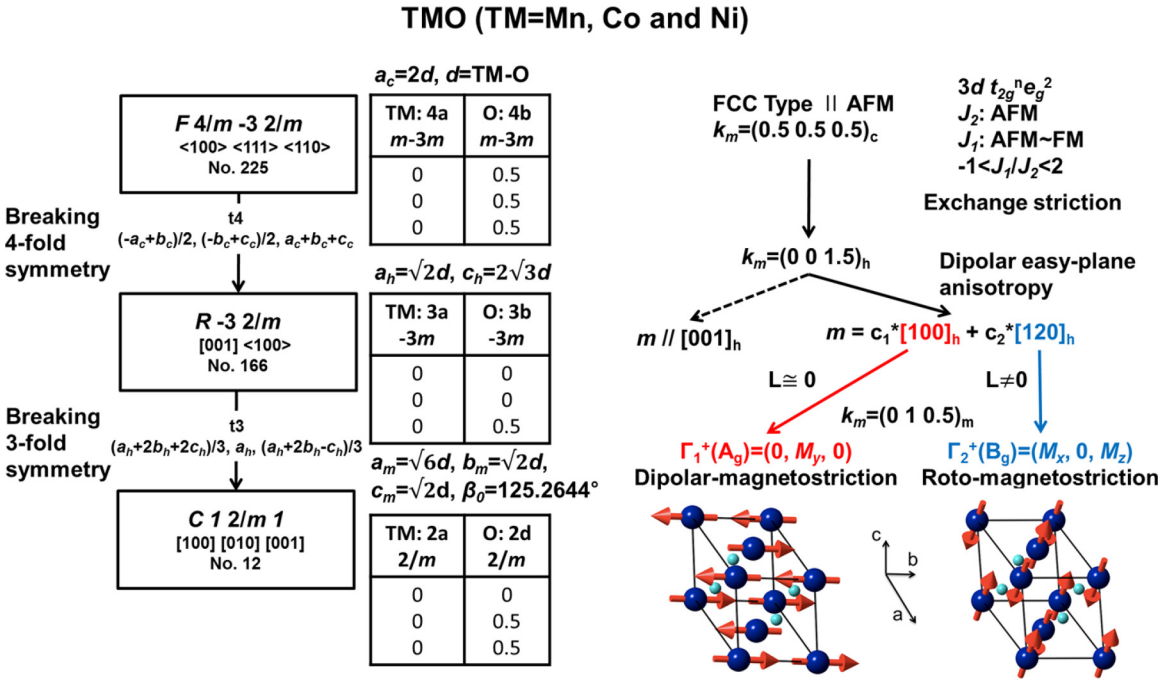

FIG. 3. Group-subgroup family tree under exchange striction and magnetostriction. Left: Crystal-structure transformation from Fm-3m to $C2/m$. Right: Magnetic propagation vector k_m, spin direction, and physical interaction.

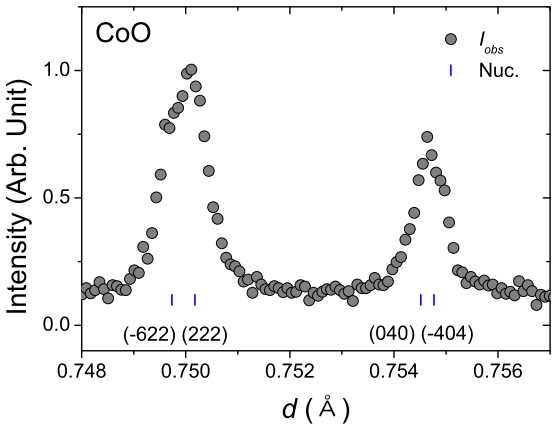

FIG. 4. Splitting of CoO monoclinic peak. High-resolution time-of-flight neutron-diffraction measurements confirm the $C2/m$ monoclinic structure as determined by x-ray tomography [23] and synchrotron-based x-ray-diffraction measurements [16]. High-resolution time-of-flight neutron powder-diffraction measurements obtained resolution comparable to that of synchrotron x-ray-diffraction measurements [48,49], which enabled us to solve the magnetic structure without confronting the problem of ferroelastic twin domains.

B. Group-subgroup structure model

As shown in Figs. 2 and 3, we constructed a group-subgroup structural relation by considering physical interaction and structure geometry on MnO, CoO, and NiO. In the simple ionic picture, TMOs have a $3d\ t_{2g}^n e_g^2$ electronic configuration inside corner sharing TMO_6 octahedra. Because of strong σ bonding between TM $3d\ e_g$ and O $2p$, the next-nearest interaction J_2 is given by a 180° superexchange interaction, which is stronger than the nearest interaction J_1. The next-nearest interaction leads to a type-II antiferromagnet; in other words, when the stability condition $-1 < J_1/J_2 < 2$ is obtained using the Green's-function technique [57], the magnetic propagation vector $k_m = (0.5\,0.5\,0.5)_c$ in a fcc cubic lattice. The parallel and antiparallel spatial distributions of spin break the fourfold crystal symmetry, which is the so-called exchange striction, and then induce the maximal subgroup R-$3m$ with magnetic propagation vector $k_m = (0\,0\,1.5)_h$ in the hexagonal lattice. The magnetic dipole-dipole interaction gives rise to easy-plane magnetic anisotropy in the R-$3m$ $(001)_h$ hexagonal plane [9], the spin directions of which compose with $[100]_h$ and $[120]_h$ as shown Fig. 2(b). Such a spin direction is incompatible with threefold crystal symmetry [6,7,17,22,58]. This spin direction induces the maximal subgroup $C2/m$ with the magnetic propagation vector $k_m = (0\,1\,0.5)_m$ in the monoclinic lattice [6].

The R-$3m$ $[100]_h$ spin direction corresponds to $\Gamma_1^+(A_g) = (0,M_y,0)$ magnetic symmetry in $C2/m$, the spin direction of which is along the monoclinic b axis, which induces normal stress perpendicular to the m_y mirror plane in $C2/m$. However, the R-$3m$ $[120]_h$ spin direction corresponds to $\Gamma_2^+(B_g) = (M_x,0,M_z)$ magnetic symmetry with initial spin angle $\theta_0 = \cos^{-1}(1/3) \approx 70.5288°$ in $C2/m$. This spin direction induces shear stress parallel to the m_y mirror plane. The $\Gamma_1^+(A_g)$ spin direction is fixed, whereas, under monoclinic distortion, the $\Gamma_2^+(B_g)$ spin direction is rotated with respect to the initial spin angle θ_0, as shown in Fig. 2(d). The dipole-dipole magnetic interaction preferences easy-plane magnetic anisotropy given by the R-$3m$ $(0\,0\,1)_h$ hexagonal plane, which selects the $\Gamma_1^+(A_g)$ spin direction with normal stress because it maintains the spin direction within the dipolar magnetic easy plane. In the $\Gamma_2^+(B_g)$ spin direction, the monoclinic distortion causes spin canting with respect to the initial θ_0. In other words, spin canting occurs with respect to the dipolar magnetic easy plane, which increases the dipole-dipole magnetic-anisotropic energy. When the energy from spin-orbit-lattice coupling compensates for the increase in energy due to the dipole-dipole magnetic anisotropy, the $\Gamma_2^+(B_g)$ spin direction is selected. Based on these physical and geometrical arguments, we expect that the quenched orbital moment $L \approx 0$ prefers the $\Gamma_1^+(A_g)$ spin direction, the so-called dipolar-magnetostriction, whereas the unquenched orbital moment $L \not\approx 0$ favors the $\Gamma_2^+(B_g)$ spin direction, which is the so-called roto magnetostriction because spin direction induces effective roto symmetry of structural distortion that will be discussed later. Dipolar magnetostriction and roto magnetostriction differ from classical magnetostriction [44]. In addition, the spin directions induced in TMOs differ.

IV. EXPERIMENTAL RESULTS AND DISCUSSIONS

A. Crystal and magnetic structure model determination

MnO has a quenched orbital moment, whereas NiO and CoO have an unquenched orbital moment [59–62]. In the present work on CoO, high-resolution neutron powder-diffraction measurements observed monoclinic peak splitting

TABLE I. Magnetic models of CoO at 60 K. Magnetic propagation vector $k_m = (0.5\ 0.5\ 0.5)_c$ in Fm-$3m$ transforms to $k_m = (0\ 1\ 0.5)_m$ in $C2/m$. The vector $k_m = (0.5\ 0.5\ 0)_m$ is inconsistent for type-II antiferromagnetism. Since $k_m = (0.5\ 0.5\ 0)_m$ gives the same bond distance between parallel and antiparallel magnetic moments in a C-centered cell, we can discard $k_m = (0.5\ 0.5\ 0)_m$ by exchange striction.

	$C2/m$, $k_m = (0\ 1\ 0.5)_m$		$C2/m$, $k_m = (0.5\ 0.5\ 0)_m$	
CoO 60 K	$\Gamma_1^+(A_g)$ $M = (0,M_y,0)$	$\Gamma_2^+(B_g)$ $M = (M_x,0,M_z)$	$\Gamma_1^+(A_g)$ $M = (0,M_y,0)$	$\Gamma_2^+(B_g)$ $M = (M_x,0,M_z)$
M_x	0	4.38(2)	0	4.70(3)
M_y	1.23(3)	0	1.63(3)	0
M_z	0	4.50 (2)	0	3.21(4)
M_{tot}	1.23(3)	4.06 (1)	1.63(3)	3.85(2)
R_{mag}	94.7	7.34	87.5	26.2

TABLE II. Magnetic models of MnO at 70 K. Monoclinic $C2/m$ with $k_m = (0\ 1\ 0.5)_m$ leads to better fits. The directions $\Gamma_1^+(A_g)$ and $\Gamma_2^+(B_g)$ are practically indistinguishable in the powder diffraction pattern. However, the $\Gamma_1^+(A_g)$ model is selected because the magnetic symmetry must differ with respect to the NiO $\Gamma_2^+(B_g)$ model.

	$R\text{-}3m$, $k_m = (0\ 0\ 1.5)_m$		$C2/m$, $k_m = (0\ 1\ 0.5)_m$	
MnO 70 K	$\Gamma_2^+(A_{2g})$ $M = (0,0,M_z)$	$\Gamma_3^+(E_g)$ $M = (M_x,M_y,0)$	$\Gamma_1^+(A_g)$ $M = (0,M_y,0)$	$\Gamma_2^+(B_g)$ $M = (M_x,0,M_z)$
M_x	0	3.90(2)	0	4.65(2)
M_y	0	0	4.12(1)	0
M_z	3.01(2)	0	0	4.03(5)
M_{tot}	3.01(2)	3.90 (2)	4.12(1)	4.07(1)
R_{mag}	25.3	14.9	8.25	5.90

as shown in Fig. 4. It confirms the $C2/m$ monoclinic structure that was already reported by high-resolution synchrotron x-ray-diffraction [16] and x-ray-tomography measurements [23]. Next, while avoiding the twin-domain problem, we clarify the $\Gamma_2^+(B_g)$ magnetic structure in CoO. As discussed in [16], the usual neutron powder diffractometer, which has poorer resolution than synchrotron x-ray diffraction, gives similar fitting results for the k_m=(0.5 0.5 0) and (0 1 0.5) magnetic propagation vector. The high-resolution neutron powder diffractometer distinguished these models as given in Table I. Also exchange striction rules out k_m=(0.5 0.5 0) physically since it gives the same Co-Co distance for antiparallel and parallel spins. However, the monoclinic distortion of MnO and NiO is too small to be detected with the current resolution of diffractometers [6,63]. Practically, tiny structural distortions such as 10^{-4}–10^{-5} Å are ignored, but any infinitely small distortions can change order-parameter direction and symmetry. Order-parameter direction and symmetry affect continuous or discontinuous phase-transition, order-parameter coupling, and domain populations whereas order-parameter amplitude distinguishes whether it is a dominant effect or not for phase transition [1,2]. These very tiny distortions within current diffractometer resolution cause unexpected discontinuous phase transition on simple ferromagnetic Ni, Fe, and Co [63,64]. This is the reason why we are concerned with monoclinic structure on MnO and NiO even though we could not find monoclinic peak splitting experimentally. Fortunately, neutron tomography [19] and neutron spherical polarimetry [12] have determined the NiO spin to be in the $[1\ 1\ -2]_p$ direction in a pseudocubic setting, which indicates the $\Gamma_2^+(B_g)$ spin direction [6]. Experiments have determined that MnO undergoes a discontinuous phase transition [31–33,35,36,42], whereas NiO undergoes a continuous phase transition [34,36,37,39,41]. Because MnO must have a different order-parameter direction and symmetry with respect to NiO, MnO has only one remaining choice, which is the $\Gamma_1^+(A_g)$ spin direction [6]. This is also consistent with the group-subgroup family tree with the quenched orbital moment ($L \approx 0$). Moreover, the $\Gamma_1^+(A_g)$ spin direction corresponds to the $[1\ 1\ 0]_p$ direction in the pseudocubic setting, as suggested

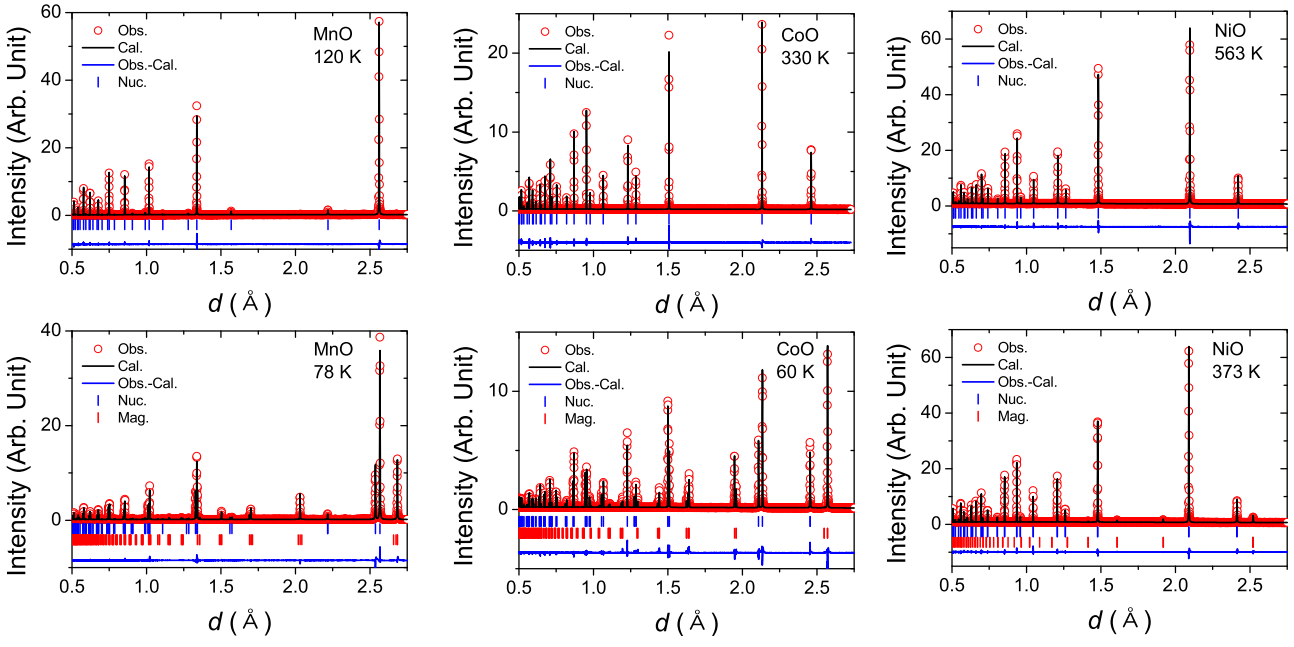

FIG. 5. Diffraction patterns and Rietveld analysis of MnO (left), CoO (middle), and NiO (right) above and below the Néel temperature.

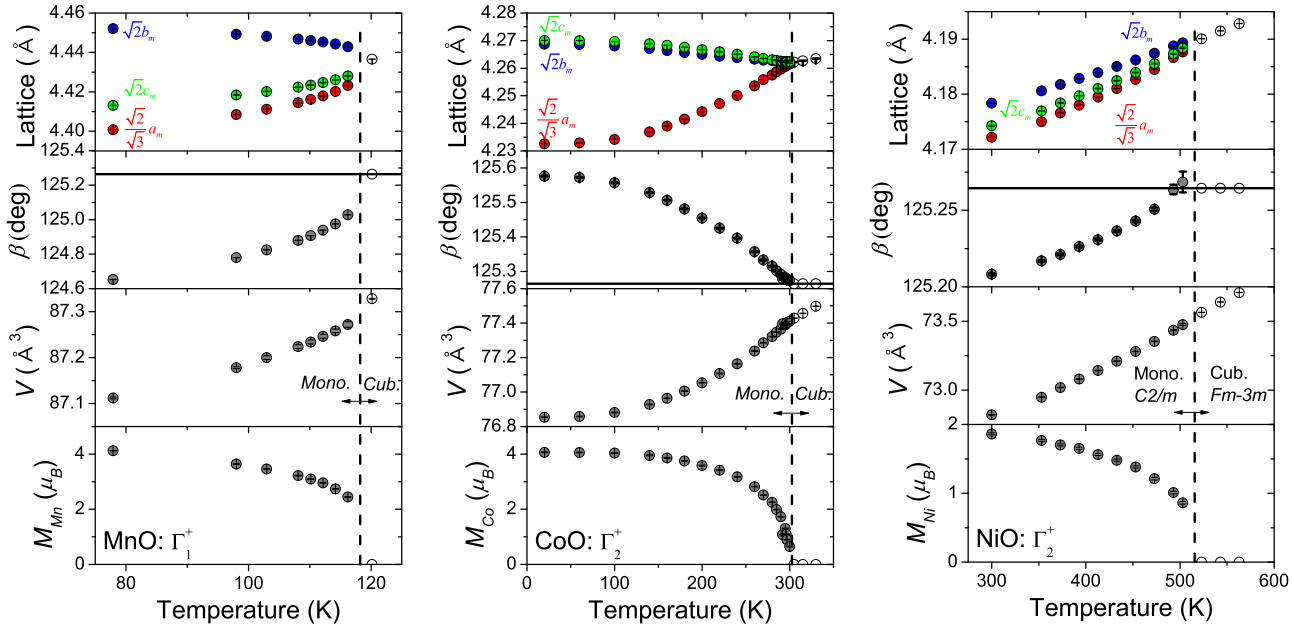

FIG. 6. Lattice constants and magnetic moments for MnO, CoO, and NiO. The vertical dashed line marks the MnO, CoO, and NiO antiferromagnetic transition at $T_N = 118$, 300, and 525 K, respectively, as determined by neutron diffraction. An antiferromagnetic transition induces a structural phase transition from cubic Fm-$3m$ to monoclinic $C2/m$, in which the monoclinic angle deviates from the initial monoclinic angle $\beta_0 = \cos^{-1}(-\frac{1}{\sqrt{3}}) \sim 125.2644^\circ$, which corresponds to the horizontal line.

by recent mPDF analysis of total neutron scattering [8]. We compared crystal and magnetic models for CoO, MnO, and NiO in Tables I and II and [6]. Finally, we choose the magnetic model for Rietveld analysis on temperature dependence, i.e., MnO is $\Gamma_1^+(A_g)$ whereas CoO and NiO are $\Gamma_2^+(B_g)$, as shown in Fig. 5. Detailed Rietveld results are given in [65].

B. Spin-direction-dependent magnetoelastic coupling

We demonstrate the temperature dependence of the lattice constant and magnetic moment for MnO, CoO, and NiO as shown in Fig. 6. For the paramagnetic Fm-$3m$ cubic phase, an alternative monoclinic setting gives an initial monoclinic angle $\beta_0 = \cos^{-1}(-1/\sqrt{3}) \approx 125.2644^\circ$ with zero magnetic moment M. Increasing the ordered magnetic moment M causes the monoclinic angle to vary as $\beta = \beta_0 \pm \Delta\beta$. Since monoclinic angle variation is a common structural order parameter for MnO, CoO, and NiO, we investigate order-parameter coupling between monoclinic angle β and polynomials in magnetic moment M as shown in Fig. 7. Then, we choose the most suitable polynomials by checking the linear

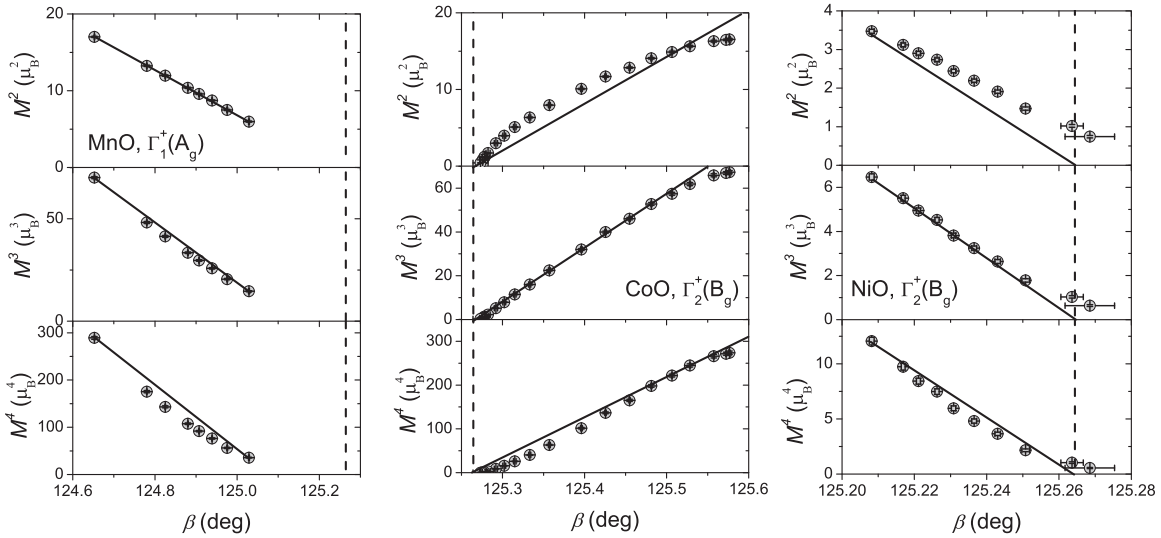

FIG. 7. Monoclinic angle β as a function of nth-order magnetic moment M^n ($n = 2$, 3, 4). The vertical dashed line marks the initial monoclinic angle $\beta_0 = 125.2644^\circ$. A straight solid line is to guide the eye. MnO shows $\beta \sim M^2$ whereas CoO and NiO show $\beta \sim M^3$.

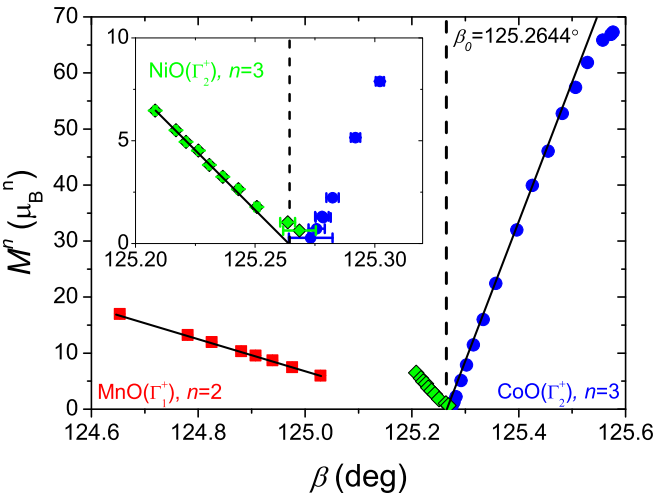

FIG. 8. Spin-direction-dependent magnetoelastic coupling in TMOs (MnO, CoO, and NiO). There are two magnetic structure, $\Gamma_1^+(A_g) = (0,M_y,0)$ and $\Gamma_2^+(B_g) = (M_x,0,M_z)$ spin directions, in $C2/m$ with magnetic propagation vector $k = (0\,1\,0.5)_m$. An order-parameter vector diagram demonstrated monoclinic angle β vs the nth-order magnetic moment M^n. MnO, CoO, and NiO are represented by red squares, blue circles, and green diamonds, respectively. Error bars are smaller than the symbol size. Inset: Expanded view of phase-transition points near β_0. Initial monoclinic angle $\beta_0 = 125.2644°$ is derived from the paramagnetic cubic Fm-$3m$ phase. The antiferromagnetic-ordered moment M induces simultaneously a monoclinic distortion $\beta = \beta_0 \pm \Delta\beta$. MnO is characterized by the $\Gamma_1^+(A_g)$ spin direction, with $\Delta\beta M^2 (n = 2)$ order-parameter coupling and a discontinuous phase transition. CoO and NiO are characterized by the $\Gamma_2^+(B_g)$ spin direction, $\Delta\beta M^3 (n = 3)$ order-parameter coupling, and a continuous phase transition. The straight line is to guide the eye.

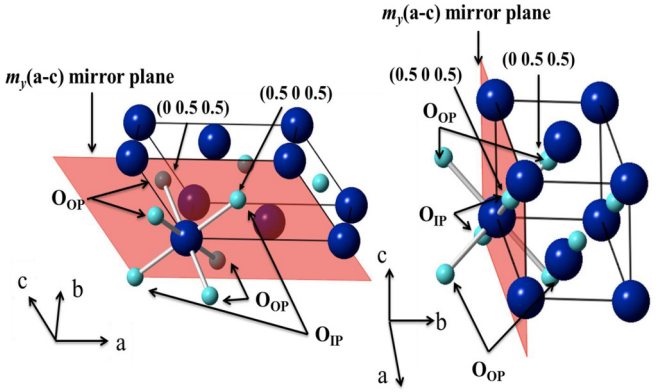

FIG. 9. Co–O bonds in $C2/m$. Six Co–O bonds split into two Co–O_{IP} bonds within the $m_y(a$–$c)$ mirror plane and four Co–O_{OP} bonds outside the $m_y(a$–$c)$ mirror plane.

relation. Finally, the order-parameter vector diagram is shown in Fig. 8.

Figure 8 and Table III classify the TMOs into two groups and show the spin-direction-dependent magnetoelastic coupling. MnO belongs to the first group, which is characterized by a quenched orbital moment ($L \approx 0$), a normal stress induced by the $\Gamma_1^+(A_g)$ spin direction, a $\Delta\beta M^2$ order-parameter coupling, and a discontinuous phase transition. Conversely, CoO and NiO belong to the second group, which is characterized by an unquenched orbital moment $L \not\approx 0$, a shear stress induced by the $\Gamma_2^+(B_g)$ spin direction, a $\Delta\beta M^3$ order-parameter coupling, and a continuous phase transition. To facilitate easy comparison of these two groups, we consider monoclinic $C2/m$ with initial β_0 instead of cubic Fm-$3m$ as the high-symmetry phase. In conventional crystallography (i.e., with neither 1* rotation-reversal symmetry nor 1′* rotation-time-reversal symmetry), monoclinic-angle deviation $\Delta\beta$ is invariant, whereas the $\Gamma_1^+(A_g)$ and $\Gamma_2^+(B_g)$ magnetic moments are variant under the 1′ time-reversal-symmetry operation. More precisely, the paramagnetic point symmetry is $G_0 = 2/m1' = \{1,2_y,-1,m_y,1',2'_y,-1',m'_y\} = H + H1'$, where H is the index-2 subgroup of G_0. The $\Gamma_1^+(A_g)$ and $\Gamma_2^+(B_g)$ magnetic structures have $H_1 = 2/m = \{1,2_y,-1,m_y\}$ and $H_2 = 2'/m' = \{1,2'_y,-1,m'_y\}$ point symmetry, respectively. In this case, the Landau free energy is approximated by expanding the order-parameter polynomial up to fourth order in the monoclinic-angle deviation $\Delta\beta$ and the magnetic moment M. Each term in the free-energy polynomial must be invariant under the 1′ time-reversal-symmetry operation:

$$F = F_0 + a_2(\Delta\beta)^2 + a_3(\Delta\beta)^3 + a_4(\Delta\beta)^4 + b_2M^2 + b_4M^4 + c_1(\Delta\beta)M^2 + c_2(\Delta\beta)^2M^2 + \cdots . \quad (3)$$

In this scenario, all TMOs have $\Delta\beta M^2$ order-parameter coupling. Under the Landau condition [1,2] of cubic-invariant $(\Delta\beta)^3$, all TMOs are expected to undergo a discontinuous phase transition. In addition, the discontinuous phase transitions are expected on the basis of the renormalization-group theory [28–30]. However, experimentally, CoO and NiO with a $\Gamma_2^+(B_g)$ magnetic structure have continuous phase transitions with the unusual order-parameter coupling $\Delta\beta M^3$, which is forbidden by 1′ time-reversal symmetry.

Because CoO exhibits a larger monoclinic distortion than MnO and NiO, high-resolution neutron powder diffraction provides data to support a detailed discussion of order-parameter coupling and the phase-transition mechanism for CoO as shown in Figs. 9–11. For the phase-transition mechanism,

TABLE III. TMO phase-transition characteristics. Spin direction, ratio L/S, stress type, order-parameter coupling, and phase-transition type. Ratio L/S with orbital moment L and spin moment S is from [59].

TMO	Spin direction	L/S	Stress induced by spin direction	Coupling	Phase transition
MnO	$\Gamma_1^+(A_g)$, $M = (0,M_y,0)$	0.00(2)	Normal	$\Delta\beta \sim M^2$	Discontinuous
CoO	$\Gamma_2^+(B_g)$, $M = (M_x,0,M_z)$	0.95(3)	Shear	$\Delta\beta(\epsilon_{oct}) \sim M^3$	Continuous
NiO	$\Gamma_2^+(B_g)$, $M = (M_x,0,M_z)$	0.34(1)	Shear	$\Delta\beta \sim M^3$	Continuous

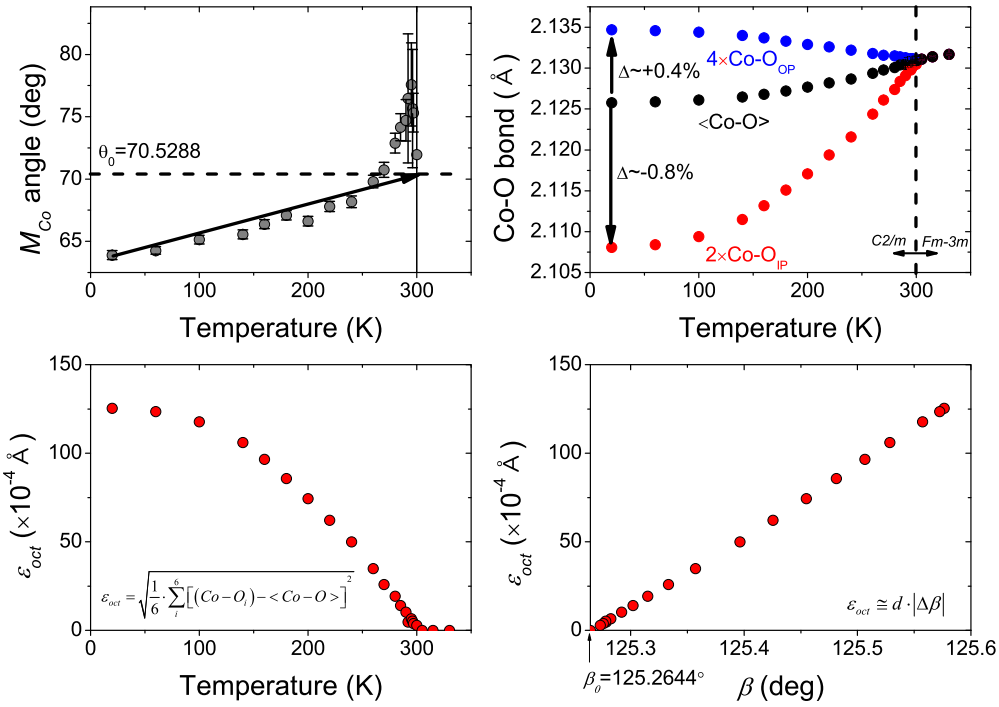

FIG. 10. CoO spin angle and bond distortion. (a) CoO spin angle as a function of temperature. The initial spin angle $\theta_0 = \cos^{-1}(1/3) \approx 70.5288^\circ$. At a low temperature, we determined the spin angle precisely with a larger monoclinic distortion than around $T_N = 300$ K. The solid line from θ to the initial θ_0 is to guide the eye. (b) Six Co–O bonds split into two Co–O_{IP} bonds within the m_y mirror plane and four Co–O_{OP} bonds outside the m_y mirror plane in $C2/m$. (c) CoO_6 octahedral distortion ϵ_{oct} as a function of temperature. (d) Octahedral distortion ϵ_{oct} as a function of $\Delta\beta$, showing the linear relationship experimentally. Because CoO lattice parameter b and c remain almost the same over the entire temperature range (as shown in Fig. 6), the octahedral distortion $\epsilon_{oct} \approx d|\Delta\beta|$, where d is the Co–O bond length in the initial cubic Fm-$3m$ lattice. Derivation process of $\epsilon_{oct} \approx d|\Delta\beta|$ is given in the Appendix.

two scenarios are proposed: classical magnetostriction [16,44] and a Jahn-Teller distortion [9,11,42,47]. Co–O bonds within CoO_6 octahedra spilt into two short Co–O_{IP} bonds within the m_y mirror plane and four long Co–O_{OP} bonds outside the m_y mirror plane, as shown in Fig. 9. The classical magnetostriction theory [44] suggests that Co spins are parallel to the short Co–O bonds in the $I4/mmm$ tetragonal structure, which corresponds to a spin angle $\theta \sim 36^\circ$ in $C2/m$. However, as shown in Fig. 10(a), high-resolution time-of-flight neutron-diffraction experiments at 20 K reveal a Co spin angle $\theta \sim 64^\circ$, which is far from the direction of the short Co–O_{IP} bond in comparison with the small angle of the monoclinic distortion of O_{OP}–Co–O_{OP} of about 0.018° from $I4/mmm$ [44].

To discuss magnetoelastic coupling in detail, we show octahedral distortion as a function of magnetic moment in CoO in Fig. 11. The CoO_6 octahedral distortion ϵ_{oct} is defined by

$$\epsilon_{oct} = \sqrt{\frac{1}{6}\sum_{i=1}^{6}[(Co-O_i)-\langle Co-O\rangle]^2} \approx d|\Delta\beta|. \qquad (4)$$

Thus, ϵ_{oct} is proportional to the variation $\Delta\beta$ in the monoclinic angle according to the monoclinic-lattice condition $b \approx c$ in the Appendix. The quantity d is the Co–O bond length in the cubic phase. To fit the entire range shown in Fig. 11, we use $\epsilon_{oct} = aM^n$ with $n = 2$, 3, 4. The $n = 2$ case clearly deviates from experimental data so the $F_{couples} \sim \epsilon_{oct}M^2$ free-energy coupling term (i.e., the Jahn-Teller distortion term) is negligible [66]. The second-lowest coupling term $F_{couples} \sim \epsilon_{oct}^2M^2$ implies that ϵ_{oct} is linear in M. This coupling term is also negligible by simple inspection. Between $n = 3$ and 4, the case $n = 3$ leads to the best fit with $a = 1.73(2) \times 10^{-4}$ Å$/\mu_B^3$ near the Néel temperature. In the inset to Fig. 11, ϵ_{oct} is linear in M^3. Far from the Néel temperature, ϵ_{oct} deviates from linearity because, probably, the effect of order-parameter saturation affects M more rapidly than ϵ_{oct} [67]. If we interpret $\epsilon_{oct} \sim M^3$ as the higher-order parameter-coupling term $F_{couples} \sim \epsilon_{oct}^2M^6$ instead of as the lower-order parameter-coupling term $F_{couples} \sim \epsilon_{oct}M^3$, then the higher-order term M^6 will cause a clear discontinuous phase transition in the order-parameter vector diagram as shown in Fig. 8. Therefore, the expansion of $F_{couples} \sim \epsilon_{oct}M^3$ with a lower-order free-energy term is more reasonable than with the higher-order term $F_{couples} \sim \epsilon_{oct}^2M^6$. In this case, CoO would reflect the free-energy coupling term $F_{couples} \sim \epsilon_{oct}M^3$, in which the odd-power magnetic moment is forbidden by $1'$ time-reversal symmetry.

To understand this unusual order-parameter coupling and the continuous phase transition in the $\Gamma_2^+(B_g)$ magnetic structure of CoO and NiO, we apply the effective roto vector symmetry to the variation $\beta = \beta_0 \pm \Delta\beta$ in the monoclinic angle. As shown in Fig. 2(d), the $\Gamma_2^+(B_g)$ spin direction can be changed with the variation $\beta = \beta_0 \pm \Delta\beta$, whereas the $\Gamma_1^+(A_g)$ spin direction remains fixed. $\Gamma_1^+(A_g)$ spin direction and $\Delta\beta$ are geometrically orthogonal whereas $\Gamma_2^+(B_g)$ and

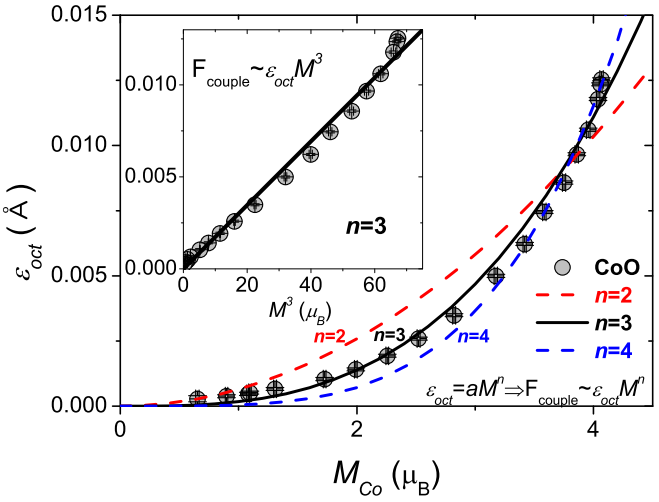

FIG. 11. The magnetoelastic coupling $\epsilon_{oct} \sim M^3$ in CoO. Gray circles show CoO octahedral distortion ϵ_{oct} as a function of Co magnetic moment M_{Co}. The solid curve is a fit over the entire range shown using an nth-order polynomial fit $\epsilon_{oct} = aM^n$. The parameter a is only a fitting parameter, whereas n is fixed. The fit with $n = 2$ (red dashed curve) clearly deviates from the data. The fit with $n = 3$ (solid curve) with $a = 1.73(2) \times 10^{-4}$ Å/μ_B^3 gives the best fit near the phase transition rather than the fit with $n = 4$ (blue dashed curve). The free energy $F_{couple} \sim \epsilon_{oct} M^3$ is forbidden by time-reversal symmetry $1'$ but allowed by rotation-time-reversal symmetry $1'^*$, as discussed in the text. Inset: The octahedral distortion ϵ_{oct} is linear in M^3. Error bars are smaller than the symbol size.

$\Delta\beta$ are inside the same mirror plane. In contrast to $\Gamma_1^+(A_g)$, $\Gamma_2^+(B_g)$ spin direction induces effective roto symmetry in $\Delta\beta$. In other words, $\Delta\beta$ has $2^*/m^*$ roto-vector symmetry, whereas the $\Gamma_2^+(B_g) = (M_x, 0, M_z)$ spin alignment has $2'/m'$ spin-vector symmetry. Instead, of a separate description of the roto vector R and spin vector S, we express their symmetry together by $2'^*/m'^*$ using $1'^*$ rotation-time-reversal symmetry breaking. Specifically, the paramagnetic point

TABLE V. Character table of the TMO order parameter in DASG. For MnO, the invariant coupling term is $\Delta\beta M^2$. For CoO and NiO, the invariant coupling term is $\Delta\beta M^3$. Because $\Delta\beta$ for MnO has total symmetry Γ_0, MnO undergoes a discontinuous phase transition dictated by the Landau condition of the invariant cubic polynomial term [2].

$2/m1'^*$	1	2_y	-1	m_y	$1'^*$	$2'^*_y$	$-1'^*$	m'^*_y	Order-parameter
Γ_0	1	1	1	1	1	1	1	1	$\Delta\beta_{Mn}$
$\Gamma_1^+(A_g)$	1	1	1	1	-1	-1	-1	-1	M_{Mn}
$\Gamma_2^+(B_g)$	1	-1	1	-1	-1	1	-1	1	M_{Co}, $\Delta\beta_{Co}$, M_{Ni}, $\Delta\beta_{Ni}$

symmetry is $G_0 = 2/m1'^* = \{1, 2_y, -1, m_y, 1'^*, 2'^*_y, -1'^*, m'^*_y\} = H + H1'^*$, where H is the index-2 subgroup of G_0 and is given by $H = 2'^*/m'^* = \{1, 2'^*_y, -1, m'^*_y\}$. The monoclinic angle $\Delta\beta$ and the magnetic moment M merge into a single irrep $A = (\Delta\beta, M)$ with respect to the $1'^*$ rotation-time-reversal symmetry. In this case, the Landau free energy is given by

$$\begin{aligned} F &= F_0 + a_2' A^2 + a_4' A^4 + \cdots \\ &= F_0 + a_2 M^2 + a_4 M^4 + a_2(\Delta\beta)^2 + a_4(\Delta\beta)^4 + c_1(\Delta\beta)M \\ &\quad + c_2(\Delta\beta)M^3 + c_3(\Delta\beta)^2 M^2 + c_4(\Delta\beta)^3 M + \cdots . \end{aligned} \quad (5)$$

This Landau free energy leads to a $\Delta\beta M^3$ coupling and a possible continuous phase transition for CoO and NiO, as shown in Fig. 8. Because ϵ_{oct} is linear in $\Delta\beta$ as a result of the monoclinic lattice condition $b \approx c$ in CoO, we can replace $\Delta\beta$ by ϵ_{oct} to finally obtain $\epsilon_{oct} \sim M^3$ in Fig. 11. Breaking the $1'^*$ rotation-time-reversal symmetry thus explains why this magnetoelastic coupling $\epsilon_{oct} \sim M^3$ is possible in CoO and why the phase transition in CoO and NiO differs from the MnO discontinuous phase transition within experimental resolution. We compare two equivalent magnetic structure descriptions between breaking time-reversal symmetry and breaking rotation-time-reversal symmetry in Table IV when the distribution of effective roto-vector properties is followed by spin distribution. When we consider the magnetoelastic

TABLE IV. Breaking of time-reversal symmetry $1'$ and rotation-time-reversal symmetry $1'^*$ in the double antisymmetry space group (DASG). We exchange atomic positions to match the DASG table format. Here, atomic positions are given by TM $2d$ (0 0.5 0.5) and O $2a$ (0 0 0) in the DASG table [4,5]. The distribution of the roto vector R follows the spin vector S distribution because we consider the situation where the spin vector induces the roto vector. We activate the phase transition from the paramagnetic phase to the antiferromagnetic phase by breaking time-reversal symmetry $1'$ and rotation-time-reversal symmetry $1'^*$. The categories represent how this space group is derived from the conventional space group [4]. In addition, we denote the DASG symbol and space-group number with the point symmetry for the transition-metal (TM) position from the DASG table [5].

Symmetry breaking	Paramagnetic SG	$\Gamma_1^+(A_g)$: (0, M_y, 0)	$\Gamma_2^+(B_g)$: (M_x, 0, M_z)
$1'$	Category 2 $Q1' = Q + Q1'$ $Q = C2/m$ $C2/m1'$ (No. 242) TM $2/m1'$	Category 3 $Q(H) = H + (Q - H)1'$ $Q = C2/m, H = C2/m$ $C(1, 1', 1')2'/m$ (No. 509) TM $2/m$	Category 3 $Q(H) = H + (Q - H)1'$ $Q = C2/m, H = C2/c$ $C(1, 1', 1')2/m'$ (No. 512) TM $2'/m'$
$1'^*$	Category 8 $Q1'^* = Q + Q1'^*$ $Q = C2/m$ $C2/m1'^*$ (No. 4505) TM $2/m1'^*$	Category 11 $Q(H)H = H + (Q - H)1'^*$ $Q = C2/m, H = C2/m$ $C(1, 1'^*, 1'^*)2'^*/m$ (No. 7154) TM $2/m$	Category 11 $Q(H)H = H + (Q - H)1'^*$ $Q = C2/m, H = C2/c$ $C(1, 1'^*, 1'^*)2/m'^*$ (No. 7157) TM $2'^*/m'^*$

coupling and phase-transition problem beyond magnetic structure, rotation-time-reversal-symmetry breaking can explain not only $\Gamma_1^+(A_g)$'s linear-quadratic magnetoelastic coupling and discontinuous phase transition but also $\Gamma_2^+(B_g)$'s linear-cubic magnetoelastic coupling and continuous phase transition. Finally, we choose the situation of breaking rotation-time-reversal symmetry in MnO, CoO, and NiO. In this case, point symmetry of the crystal and magnetic order parameter is summarized in Table V. Still, Landau free energy of $\Gamma_1^+(A_g)$ is given by the same Eq. (3).

V. CONCLUSION

$\Gamma_1^+(A_g)$ and $\Gamma_2^+(B_g)$ spin directions lead distinguished order-parameter coupling $\Delta\beta \sim M^2$ and M^3, discontinuous and continuous phase transitions, respectively, for MnO, CoO, and NiO. For the CoO phase-transition mechanism, classical magnetostriction and Jahn-Teller distortion are denied by precise spin direction and the magnetoelastic coupling $\epsilon_{\rm oct} \sim M^3$ which is forbidden by time-reversal symmetry. We apply rotation-time-reversal symmetry to explain order-parameter coupling and continuous phase transition in the $\Gamma_2^+(B_g)$ spin direction of CoO and NiO. We introduced a type of magnetostriction, i.e., dipolar magnetostriction and roto magnetostriction. Our experimental result and interpretation succeed to explain the long-standing problem of spin directions and the phase-transition mechanism in transition-metal monoxide. Moreover, this is experimental evidence of general symmetry of the magnetic moment that magnetic moment and static structural distortion can belong to the same irreducible representation, which was impossible under time-reversal symmetry. This experimental discovery opens a way to find the physical phenomena which was prohibited by time-reversal symmetry but allowed by rotation-time-reversal symmetry in condensed matter physics.

ACKNOWLEDGMENTS

We are grateful to Masahiro Shioya, Katsumi Shimizu, and Takashi Muroya for their technical support at the SuperHRPD beamline at the Materials and Life Science Experimental Facility, J-PARC. The neutron-diffraction experiments using SuperHRPD were carried out under S-type project with Proposal No. 2014S10.

APPENDIX: CoO_6 OCTAHEDRAL DISTORTION

The initial alternative monoclinic $C2/m$ settings for cubic $Fm\text{-}3m$ are

$$a_0 = \sqrt{6}d, \quad b_0 = \sqrt{2}d, \quad c_0 = \sqrt{2}d, \quad \alpha = \gamma = 90^\circ,$$
$$\beta_0 = \cos^{-1}\left(-\frac{1}{\sqrt{3}}\right) \approx 125.2644^\circ. \tag{A1}$$

Next, antiferromagnetic order induces a monoclinic distortion whereby each lattice constant deviates by $x = x_0 \pm \Delta x$ from their initial value of x_0. To begin, we derive the relationship between the lattice constant and the deviation in monoclinic angle using trigonometric functions and differentiation:

$$\cos(\beta) = \cos(\beta_0 + \Delta\beta)$$
$$\approx \cos(\beta_0) - \sin(\beta_0)\Delta\beta = -\frac{1}{\sqrt{3}} - \frac{\sqrt{2}}{\sqrt{3}}\Delta\beta, \tag{A2}$$
$$\text{diff}\left(\cos(\beta) = -\frac{c}{a}\right)$$
$$-\sin(\beta_0)\Delta\beta = -\frac{a_0\Delta c - c_0\Delta a}{a_0^2}, \tag{A3}$$
$$\frac{\Delta a}{\sqrt{6}} = \frac{\Delta c}{\sqrt{2}} - \sqrt{2}d\Delta\beta,$$

The initial cubic phase includes six Co–O bond lengths, being d split into two short Co–O_{IP} bonds with bond length d_{IP} within the m_y (a–c) mirror plane and four long Co–O_{OP} bonds with bond length d_{OP} outside the m_y (a–c) mirror plane in $C2/m$. Co–O_{OP} bonds with bond length d_{OP} are derived from the distance between the positions of Co (0 0 0) and O_{OP} (0 0.5 0.5) with the approximation $d \gg \Delta b, \Delta c$:

$$d_{OP} = \sqrt{(0.5b)^2 + (0.5c)^2}$$
$$= 0.5\sqrt{(\sqrt{2}d + \Delta b)^2 + (\sqrt{2}d + \Delta c)^2}$$
$$\approx d + \frac{1}{2\sqrt{2}}(\Delta b + \Delta c). \tag{A4}$$

In addition, the Co–O_{IP} bond with bond length d_{IP} can be derived from the distance between Co (0 0 0) and O_{IP} (0.5 0 0.5) by considering the limit $d \gg \Delta b, \Delta c$ and Eqs. (A2) and (A3). The result is

$$d_{IP} = \sqrt{(0.5a)^2 + (0.5c)^2 + 2(0.5a)(0.5c)\cos(\beta)}$$
$$= 0.5\sqrt{(\sqrt{6}d + \Delta a)^2 + (\sqrt{2}d + \Delta c)^2 + 2(\sqrt{6}d + \Delta a)(\sqrt{2}d + \Delta c)\left(-\frac{1}{\sqrt{3}} - \frac{\sqrt{2}}{\sqrt{3}}\Delta\beta\right)}$$
$$\approx d + \frac{1}{\sqrt{2}}\Delta c - \frac{3\sqrt{2}}{2}d\Delta\beta. \tag{A5}$$

In $C2/m$, the mean Co–O bond length $d_{\rm mean}$ is given by

$$d_{\rm mean} = \frac{4d_{OP} + 2d_{IP}}{6}$$
$$\approx d + \frac{1}{3\sqrt{2}}(\Delta b + 2\Delta c) - \frac{\sqrt{2}}{2}d\Delta\beta. \tag{A6}$$

We calculate the octahedral distortion $\epsilon_{\rm oct}$ as follows:

$$d_{OP} - d_{\rm mean} = \frac{\sqrt{2}}{2}d\Delta\beta + \frac{1}{6\sqrt{2}}(\Delta b - \Delta c), \tag{A7}$$
$$d_{IP} - d_{\rm mean} = -\sqrt{2}d\Delta\beta + \frac{1}{3\sqrt{2}}(\Delta c - \Delta b), \tag{A8}$$

$$\epsilon_{\rm oct} = \sqrt{\frac{4(d_{\rm OP} - d_{\rm mean})^2 + 2(d_{\rm IP} - d_{\rm mean})^2}{6}}. \quad \text{(A9)}$$

When the CoO monoclinic lattice parameters b and c are almost the same over the entire temperature, as shown in Fig. 6, the CoO_6 octahedral distortion $\epsilon_{\rm oct}$ is proportional to the variation $\Delta\beta$ in the monoclinic angle, as shown by the experimental results reported in Fig. 10(d), and as given by

$$\epsilon_{\rm oct} \approx d|\Delta\beta|. \quad \text{(A10)}$$

[1] L. Landau, Zh. Eksp. Teor. Fiz. **7**, 19 (1937) [Phys. Z. Sowjetunion **11**, 26 (1937)].
[2] J. C. Tolédano and P. Tolédano, *The Landau Theory of Phase Transition* (World Scientific, Singapore, 1987).
[3] V. Gopalan and D. B. Litvin, Nat. Mater. **10**, 376 (2011).
[4] B. K. VanLeeuwen, V. Gopalan, and D. B. Litvin, Acta Cryst. A **70**, 24 (2014), double antisymmetry space group, http://sites.psu.edu/gopalan/research/symmetry/.
[5] M. Huang, B. K. VanLeeuwen, D. B. Litvin, and V. Gopalan, Acta Cryst. A **70**, 373 (2014).
[6] S. Lee, Y. Ishikawa, P. Miao, S. Torii, and T. Kamiyama, JPS Conf. Proc. **8**, 034007 (2015).
[7] J. M. Perez-Mato, S. V. Gallego, E. S. Tasci, L. Elcoro, G. de la Flor, and M. I. Aroyo, Annu. Rev. Mater. Res. **45**, 217 (2015).
[8] B. A. Frandsen and S. J. L. Billinge, Acta Cryst. **A71**, 325 (2015).
[9] A. Schrön, C. Rödl, and F. Bechstedt, Phys. Rev. B **86**, 115134 (2012).
[10] M. A. Carpenter, Z. Zhang, and C. J. Howard, J. Phys. Condes. Matter **24**, 156002 (2012).
[11] K. Siratory and K. Kohn, J. Phys. Soc. Jpn. **79**, 114720 (2010).
[12] E. Ressouche, N. Kernavanois, L.-P. Regnault, and J.-T. Henry, Physica B **385-386**, 394 (2006).
[13] A. L. Goodwin, M. G. Tucker, M. T. Dove, and D. A. Keen, Phys. Rev. Lett. **96**, 047209 (2006).
[14] A. P. Kantor, L. S. Dubrovinsky, N. A. Dubrovinskaia, I. Y. Kantor, and I. N. Goncharenko, J. Alloys. Compd. **402**, 42 (2005).
[15] K. Tomiyasu, T. Inami, and N. Ikeda, Phys. Rev. B **70**, 184411 (2004).
[16] W. Jauch, M. Reehuis, H. J. Bleif, F. Kubanek, and P. Pattison, Phys. Rev. B **64**, 052102 (2001).
[17] H. Shaked, J. Faber, Jr., and R. L. Hitterman, Phys. Rev. B **38**, 11901 (1988).
[18] A. K. Cheetham and D. A. O. Hope, Phys. Rev. B **27**, 6964 (1983).
[19] J. Baruchel, M. Schlenker, K. Kurosawa, and S. Saito, Philos. Mag. B **43**, 853 (1981).
[20] R. Bidaux, R. Conte, and J. A. Nasser, J. Phys. **41**, 1317 (1980).
[21] D. Herrmann-Ronzaud, P. Burlet, and J. Rossat-Mignod, J. Phys. C **11**, 2123 (1978).
[22] A. P. Cracknell and S. J. Joshua, Proc. Camb. Phil. Soc. **66**, 493 (1969).
[23] S. Saito, K. Nakahigashi, and Y. Shimomura, J. Phys. Soc. Jpn. **21**, 850 (1966).
[24] W. L. Roth, Phys. Rev. **110**, 1333 (1958).
[25] C. G. Shull, W. A. Strauser, and E. O. Wollan, Phys. Rev. **83**, 333 (1951).
[26] C. G. Shull and J. S. Smart, Phys. Rev. **76**, 1256 (1949).
[27] A. P. Cracknell, M. F. Cracknell, and B. L. Davies, Phys. Stat. Sol. **39**, 463 (1970).
[28] S. A. Brazovskii and I. E. Dzyaloshinskii, ZhETF Pis. Red. **21**, 360 (1975) [JETP Lett. **21** 164 (1975)].
[29] D. Mukamel and S. Krinsky, Phys. Rev. B **13**, 5078 (1976).
[30] P. Bak, S. Krinsky, and D. Mukamel, Phys. Rev. Lett. **36**, 52 (1976).
[31] D. Bloch and R. Maury, Phys. Rev. B **7**, 4883 (1973).
[32] D. Bloch, R. Maury, C. Vetter, and W. B. Yelon, Phys. Lett. **49**, 354 (1974).
[33] D. Bloch, D. Hermann-Ronzaud, and C. Vettier, Phys. Rev. Lett. **35**, 963 (1975).
[34] C. F. V. Doorn and P. de. V. Du Plessis, Phys. Lett. A **66**, 141 (1978).
[35] M. S. Jagadeesh and M. S. Seehra, Phys. Rev. B **23**, 1185 (1981).
[36] G. Srinivasan and M. S. Seehra, Phys. Rev. B **28**, 6542 (1983).
[37] G. Srinivasan and M. S. Seehra, Phys. Rev. B **29**, 6295 (1984).
[38] F. Romero, J. Jiménez, and J. Del Cerro, J. Magn. Magn. Mater. **280**, 257 (2004).
[39] M. Massot, A. Oleaga, A. Salazar, D. Prabhakaran, M. Martin, P. Berthet, and G. Dhalenne, Phys. Rev. B **77**, 134438 (2008).
[40] A. Oleaga, A. Salazar, and E. H. Bocanegra, Phys. Rev. B **80**, 024426 (2009).
[41] T. Chatterji, G. J. McIntyre, and P.-A. Lindgard, Phys. Rev. B **79**, 172403 (2009).
[42] C. Kant, F. Mayr, T. Rudolf, M. Schmidt, F. Schrettle, J. Deisenhofer, and A. Loidl, Eur. Phys. J. Special Topics **180**, 43 (2010).
[43] S. Greenwald and J. S. Smart, Nature (London) **166**, 523 (1950).
[44] J. Kanamori, Prog. Theor. Phys. **17**, 197 (1957).
[45] B. Morosin, Phys. Rev. B **1**, 236 (1970).
[46] L. Bartel and B. Morosin, Phys. Rev. B **3**, 1039 (1971).
[47] K. I. Kugel and D. Khomskii, Sov. Phys. Usp. **25**, 231 (1982).
[48] S. Torii, M. Yonemura, T. Yulius Surya Panca Putra, J. Zhang, P. Miao, T. Muroya, R. Tomiyasu, T. Morishima, S. Sato, H. Sagehashi *et al.*, J. Phys. Soc. Jpn. **80**, SB020 (2011).
[49] S. Torii, M. Yonemura, Y. Ishikawa, P. Miao, R. Tomiyasu, S. Satoh, Y. Noda, and T. Kamiyama, J. Phys.: Conf. Ser. **502**, 012052 (2014).
[50] R. Oishi, M. Yonemura, Y. Nishimaki, S. Torii, A. Hoshikawa, T. Ishigaki, T. Morishima, K. Mori, and T. Kamiyama, Nucl. Instr. Meth. Phys. Res. A **600**, 94 (2009).
[51] R. Oishi-Tomiyasu, M. Yonemura, T. Morishima, A. Hoshikawa, S. Torii, T. Ishigaki, and T. Kamiyama, J. Appl. Cryst. **45**, 299 (2012).
[52] J. Rodríguez-Carvajal, Phys. B Condens. Matter **192**, 55 (1993).
[53] A. Wills, Phys. B Condens. Matter **276**, 680 (2000).
[54] M. I. Aroyo, A. Kirov, C. Capillas, J. Perez-Mato, and H. Wondratschek, Acta Cryst. A **62**, 115 (2006).
[55] *International Tables for Crystallography, Symmetry Relations Between Space Groups*, edited by U. M. H. Wondratschek, 1st ed. (Kluwer Academic, New York, 2004), Vol. A1, Chap. 3.

[56] A. N. Morozovska, V. V. Khist, M. D. Glinchuk, V. Gopalan, and E. A. Eliseev, Phys. Rev. B **92**, 054421 (2015).
[57] L. Bartel, Solid State Commun. **11**, 55 (1972).
[58] J. Rodríguez-Carvajal and F. Bourée, EPJ Web of Conferences **22**, 00010 (2012).
[59] W. Neubeck, C. Vettier, F. De Bergevin, F. Yakhou, D. Mannix, L. Ranno, and T. Chatterji, J. Phys. Chem. Solids **62**, 2173 (2001).
[60] V. Fernandez, C. Vettier, F. de Bergevin, C. Giles, and W. Neubeck, Phys. Rev. B **57**, 7870 (1998).
[61] W. Neubeck, C. Vettier, V. Fernandez, F. De Bergevin, and C. Giles, J. Appl. Phys. **85**, 4847 (1999).
[62] S. K. Kwon and B. I. Min, Phys. Rev. B **62**, 73 (2000).
[63] S. Yang and X. Ren, Phys. Rev. B **77**, 014407 (2008).
[64] S. Yang, X. Ren, and X. Song, Phys. Rev. B **78**, 174427 (2008).
[65] See Supplemental Material at http://link.aps.org/supplemental/10.1103/PhysRevB.93.064429 for details of Rietveld results tables.
[66] E. Salje and M. Carpenter, J. Phys. Condens. Matter **23**, 462202 (2011).
[67] E. Salje, B. Wruck, and H. Thomas, Z. Phys. B Con. Mat. **82**, 399 (1991).